Available online at www.sciencedirect.com
SCIENCE DIRECT®
Engineering Fracture Mechanics 72 (2005) 2721–2743
Engineering Fracture Mechanics
www.elsevier.com/locate/engfracmech

Dynamic crack growth in particulate bimaterials having discrete and diffuse interfaces: Role of microstructure

R. Kitey, H.V. Tippur *

Department of Mechanical Engineering, 202 Ross Hall, Auburn University, Alabama 36849, USA

Received 10 January 2005; received in revised form 22 June 2005; accepted 4 July 2005
Available online 1 September 2005

Abstract

Role of microstructure on interfacial crack growth in particulate bimaterials made of glass particle reinforced epoxy is examined experimentally. Two types of bimaterials, one with a discrete jump in mean filler particle size across the interface and the other with two intermixed particle sizes in the interfacial region, are studied. The choice of particle sizes used in bimaterials is based on a set of experiments in which particle size effects on fracture behavior of monolithic specimens with single particle size are established using optical interferometry and high-speed photography. A non-monotonic steady state stress intensity factor (K_{Iss}) variation with mean particle size is observed in the size range of 7–203 μm for 10% volume fraction. Among the selected particles sizes, 35 μm mean diameter is found to produce the highest K_{Iss}. Increasing or decreasing particle size results in measurable reduction in K_{Iss} of the composite. Based on this result, discrete and diffuse bimaterials made of 35 μm and 203 μm diameter filler particles are studied. The K_{Iss} of the diffuse interface with intermixed particle sizes is bounded by the ones for monolithic configurations with single size particles. Further, K_{Iss} appears to vary linearly with the volume fraction of particle size having lower K_{Iss} in monolithic configurations. On the contrary, in case of a microstructurally discrete interface, the measured K_{Iss} is same as the one for the weaker half of the bimaterial.

Keywords: Particulate composites; Matrix reinforcement; Optical measurements; Dynamic crack growth; Interfacial failure; Microstructure; Size effect

* Corresponding author. Tel.: +1 334 844 3327; fax: +1 334 844 3307.
E-mail address: htippur@eng.auburn.edu (H.V. Tippur).

0013-7944/$ - see front matter © 2005 Elsevier Ltd. All rights reserved.
doi:10.1016/j.engfracmech.2005.07.006

1. Introduction

Layered material systems with discrete and diffuse interfaces are encountered in a number of engineering applications, from microelectronics to aircraft engines. Interfacial failure due to design, manufacturing and/or service related issues are inherent to these material systems. Among the various scenarios, two situations can be commonly recognized under dominant tensile loading conditions. First, when the interface is strong relative to the individual components of the layered system, cracks tend to kink into the weaker material and grow nearly parallel to the interface [1]. In this situation fracture properties of the weaker material becomes the limiting value for deciding overall fracture toughness. The second situation corresponds to a relatively weaker interface wherein crack initiation and propagation occurs along the interface. Here, the interfacial characteristics control overall fracture parameters. Most works to date in these categories deal with elastically dissimilar interfaces characterized by an oscillatory inverse square-root of r singularity [2]. New literature on the topic has widened the understanding of interfacial crack tip fields, crack initiation and crack growth behaviors in bimaterials with discrete interfaces [3,4]. Quasi-static fracture toughness and mode mixities for various material combinations have been reported by several investigators [5–7]. The challenges of investigating dynamic fracture in bimaterial interfaces have also been overcome in the past. The work of Tippur and Rosakis [8] on dynamic crack growth in PMMA–aluminum bimaterials identified interesting interfacial fracture characteristics such as crack speeds approaching the wave speed of the compliant constituent of the bimaterial. Other investigators have subsequently reported analytical [9,10], numerical [11,12] and experimental [10,13] studies adding a wealth of new knowledge including possibilities of intersonic and supersonic interfacial crack growth, occurrence of shock waves, etc.

Discrete bimaterial interfaces can be considered as a subset of layered material systems having non-homogeneous interfacial regions within which material characteristics transition from that of one constituent to the other in a predetermined fashion. This aids in mitigating deficiencies of discrete interfaces with a sudden transition in material characteristics often at the root of problems in discretely layered systems [14–16]. In practice, such diffuse and/or graded interfacial regions typically include two microscopically intermixed constituents. The relative proportions of the two constituents in the interfacial region are varied to suit a given thermo-mechanical environment by producing microstructural or compositional variations via plasma spraying, screw extrusion, sintering, gravity and centrifugal castings, etc. [17–19]. Such microstructural variations influence not only elastic characteristics but the failure behavior as well. However, focus in the past has been either on elastic mismatch or combinations of elastic and failure mismatches [16,20,21] and the role of microstructure in governing the fracture behavior of bimaterials has not been fully investigated.

Understanding the fracture mechanics of discrete and diffuse interfaces is relevant in other situations as well. Particulate sizes could show sudden or gradual variations in cementitious materials when constituents from multiple sources are used or curing conditions are varied during construction. This is a common occurrence in this class of materials since the aggregate sizes are not tightly controlled and vary over a range [22–24]. Another situation where microstructurally dissimilar interfaces occur include heat affected zones, where grain size/shape variations occur. Geological formations across the fault lines correspond to a much larger scale example of interfaces with microstructural variations. Lastly, there exists a strong interest towards functionalizing interfaces with nanophases to enhance failure characteristics. Fracture mechanics modeling of any of these scenarios requires an understanding of the role microstructure plays at an interface of a discrete or diffuse variety. Particularly, questions relevant to (a) whether particle size bimodality would enhance or diminish interfacial fracture toughness, (b) crack path selection in discrete interfaces, must be explored. Therefore, in this study dynamic fracture behavior of elastically similar bimaterials having discrete and diffuse interfaces are considered. Polymeric matrix with solid glass filler provide a cost-effective method for modeling fracture behavior of microstructurally dissimilar interfaces under laboratory conditions. The availability of a wide range of particle sizes of spherical shape makes such a study feasible.

As a first step, understanding the role filler particle size plays on fracture behavior of monolithic configurations is essential. The filler size effect on failure characteristics for the case of static loading have been addressed in previous studies and dynamic counterparts are still largely absent. Spanoudakis and Young [25,26] have shown that critical stress intensity factor (K_{Ic}) decreases with an increase in particle size at lower volume fractions, while the critical energy release rate (G_{Ic}) drops with increasing particle size to a minimum value at 47 μm particle diameter. The speculating toughening mechanisms were crack pinning followed by particle–matrix interface failure and crack tip blunting due to the break down of particle–matrix interfaces. Moloney et al. [27] investigated 40% volume fraction silica-filled epoxy with particle size in the range of 60–300 μm. Negligible effect of particle size was observed on fracture toughness. Nakamura et al. [28] investigated particle size effect on fracture properties for 35% volume fraction for 2–30 μm spherical silica-filled epoxy. The decrease in K_{Ic} with a decrease in particle size was noticed, which further was attributed to the differences in crack deflection, interfacial debonding and particle fracture. In a similar investigation [29] on silica-filled epoxy with particle size range of 2–42 μm (55% and 64% weight fraction), both fracture toughness and energy released rate were reported to have decreased with a decrease in particle size. Evidently, the conclusions drawn contain notable differences. While some have reported an increase in K_{Ic} as particle size decreases, others have reported either a decreasing trend or no effect at all. Hence, it is necessary to investigate particle size effect on fracture toughness, particularly over a relatively large range of particle sizes, prior to examining microstructural influences on interfacial fracture.

In this work first solid glass spheres of various sizes in the range of 7–200 μm in diameters are used to study particle size effect on fracture behavior of macroscopically homogeneous glass-filled epoxy sheets under impact loading conditions. Crack initiation and growth as well as crack tip deformations are measured. The measurements are used to determine macroscopic fracture parameters. Subsequently, two filler sizes which give the largest mismatch in fracture toughness yet have similar macroscopic elastic properties, are selected to prepare bimaterial interfaces. A separate set of experiments involving bimaterials with discrete and diffuse interfaces are used to study microstructural effects on interfacial failure.

2. Material preparation and characterization

2.1. Monolithic specimens

Glass-filled (*solid* A-glass spheres[1] bulk density 2500 kg/m^3) epoxy specimens with 10% filler volume fraction are used in this study. The relatively low V_f could assist in avoiding agglomeration problems yet high enough for influencing fracture properties. Uncoated or ''as-is'' glass spheres of mean diameters 7 μm, 11 μm, 35 μm, 71 μm and 203 μm have been used to study filler size effects. Low viscosity epoxy,[2] prepared by mixing Bisphenol-A resin and Amine based hardener (densities 1130 kg/m^3 and 961 kg/m^3) in the ratio of 100:36, was used as the matrix material. Epoxy and glass particles were mixed until partially gelled before being poured into a mold and cured at room temperature for approximately 72 h. Physical and elastic properties of the resulting glass-filled epoxy composites are tabulated in Table 1. Longitudinal and shear wave speeds (C_l and C_s) were measured by ultrasonic *pulse–echo* transducers at discrete locations of the cured material. Transit time for the pulse to travel twice the thickness of the sample was measured with the help of longitudinal and shear wave transducers separately. Dynamic elastic modulus E_d and Poisson's ratio v_d were calculated after independently measuring the mass density ρ of the composite and using,

[1] Soda-Lime glass (Composition %: SiO_2—72.5, Na_2O—13.7, CaO—9.8, MgO—3.3, Al_2O_3—0.4, FeO/Fe_2O_3—0.2, K_2O—0.1), Spheriglass, Potters Industries Inc.

[2] Epo-Thin, Buehler Inc., USA (pre-2003 formulation).

Table 1
Measured material properties of uncoated glass-filled epoxy, V_f—0.1

Average particle diameter D (μm)	Density ρ (kg/m^3)	Longitudinal wave speed C_l (m/s)	Shear wave speed C_s (m/s)	Elastic modulus E_d (MPa)	Poisson's ratio v_d
203	1279	2567	1174	4829	0.37
71	1282	2585	1182	4902	0.37
35	1296	2550	1172	4871	0.37
11	1291	2561	1188	4973	0.36
7	1298	2581	1183	4968	0.37
Epoxy	1132	2468	1109	3824	0.37
203 + 35	1292	2536	1173	4849	0.36
203 + 11	1278	2558	1175	4822	0.37

$$C_l = \sqrt{\frac{E_d(1-v_d)}{\rho(1+v_d)(1-2v_d)}}, \quad C_s = \sqrt{\frac{E_d}{2\rho(1+v_d)}}. \tag{1}$$

From Table 1 it can be noticed that E_d and v_d remain unaffected by the filler size variation. Average values for E_d and v_d were found to be 4.85 GPa and 0.365 respectively. Cast sheets were machined into test samples of dimensions 152 mm × 42 mm × 8 mm for optical study. The surface was first roughened with 150 grit sand paper. Subsequently, the surface was made optically flat and specular by transferring a thin (a few nm thick) aluminum film using an optical flat and a layer of epoxy. An edge notch of root radius 150 μm and nominal length of 10 mm was cut into the sample using a high-speed diamond impregnated circular saw. In case of bimaterial samples (to be discussed next), notch was cut along the interface at the middle of the specimen.

2.2. Bimaterial specimens

Two different filler sizes were used in the preparation of bimaterials. Evenly mixed glass-fillers were dispersed in epoxy as described earlier for monolithic specimens. Two limiting cases have been considered in this study. In the first case, the interfacial region is "large" ($L/D \to \infty$, L and D being the interface length and particle size, respectively) when compared to particle sizes and in the second case, the interfacial region is vanishingly narrow ($L/D \to 0$). These two cases are also referred to as *diffuse* and *discrete* interfaces, respectively, and are shown schematically in Fig. 1. To prepare a bimaterial with a discrete interface, one-half of the mold was poured first with a mixture containing larger size particles of 203 μm mean diameter at 10% V_f. After the material was cured, a glass–epoxy mixture containing smaller particles (either 35 μm or 11 μm) at 10% V_f was cast on top of (or, adjacent to) the cured sheet. Preparation of a bimaterial with diffuse interface was similar to the discrete interface preparation but for casting the interface material centrally in between two cured (macroscopically) homogeneous halves. In this case, the diffuse interfacial region contains 5% V_f of larger and 5% V_f of smaller particles.

3. Optical method and measurements

The optical method of coherent gradient sensing, CGS [30], in conjunction with high-speed photography was used to study crack tip deformations. CGS measures in-plane gradients of out-of-plane surface displacements (surface slopes) around a crack tip when used to study opaque solids. A schematic of the experimental set-up of reflection CGS is shown in Fig. 2. A collimated beam of coherent laser light illuminates an

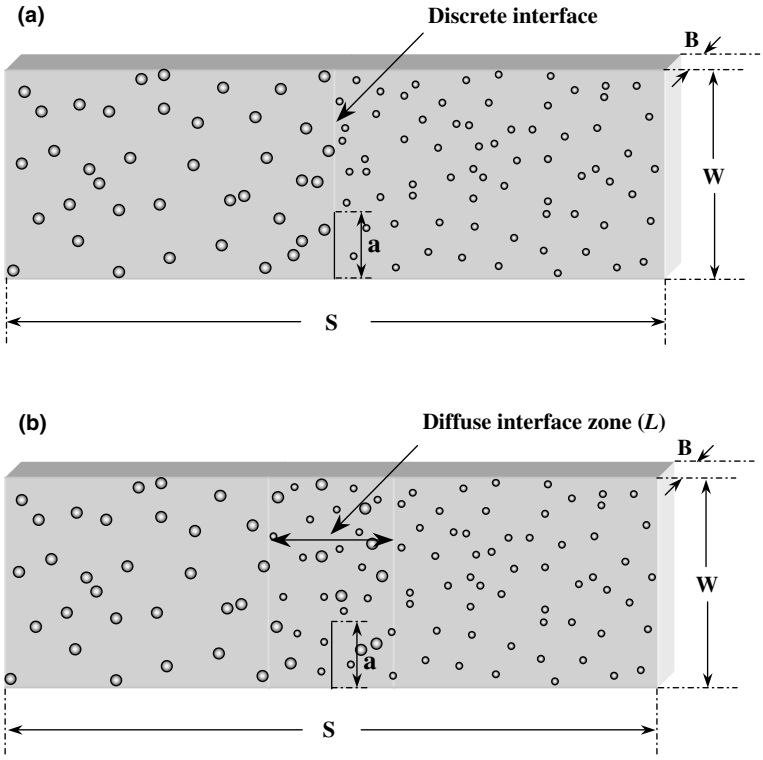

Fig. 1. Schematic showing discrete and diffuse interfacial regions for a particulate bimaterial: (a) discrete interface ($L/D \to 0$), and (b) diffuse interface ($L/D \to \infty$), D: mean particle diameter.

opaque specimen with a specularly reflective surface. The reflected object wave front is incident on a pair of high-density Ronchi gratings G_1 and G_2, spatially separated by a distance Δ, as shown. The parallel gratings diffract the object wave-front successively in several discrete directions. The filtering lens L collects the light field and displays its frequency content on its back focal plane as a series of diffraction spots. By locating a filtering aperture around ± 1 diffraction order, the information about surface slopes in the form of interference fringes is captured at the image plane. The optical set-up requires the imaging system to be focused on the object surface.

The experimental set-up includes an impactor, a pulse laser, CGS interferometer and a continuous access high-speed camera. An Argon-ion laser beam (wavelength $\lambda = 514$ nm) is expanded and collimated into a 50 mm diameter beam. A pneumatically operated cylindrical steel hammer with hemispherical tip is used to impact (velocity 5.3 m/s) the center of the specimen along the negative x-axis, as shown in the schematic. The specimen is initially rested on two soft-putty blocks to simulate free–free support conditions. Before the impactor hits the specimen, a flag triggers a photo-detector, which in turn opens a capping shutter in front of the camera. This allows laser beam to expose a strip of photographic film located in a circular track within the camera. As soon as the impactor touches an adhesive backed copper tape fixed on the top edge of the specimen, an electrical circuit initiates a gate pulse of 320 μs duration. Laser pulses of 50 ns width are repeated at 5 μs intervals (200,000 fps) during the gate period. With these settings, approximately 70 images are exposed onto the film. The incident beam upon reflecting from the deformed surface carries information about the non-planarity of the surface near the crack tip and the impact point.

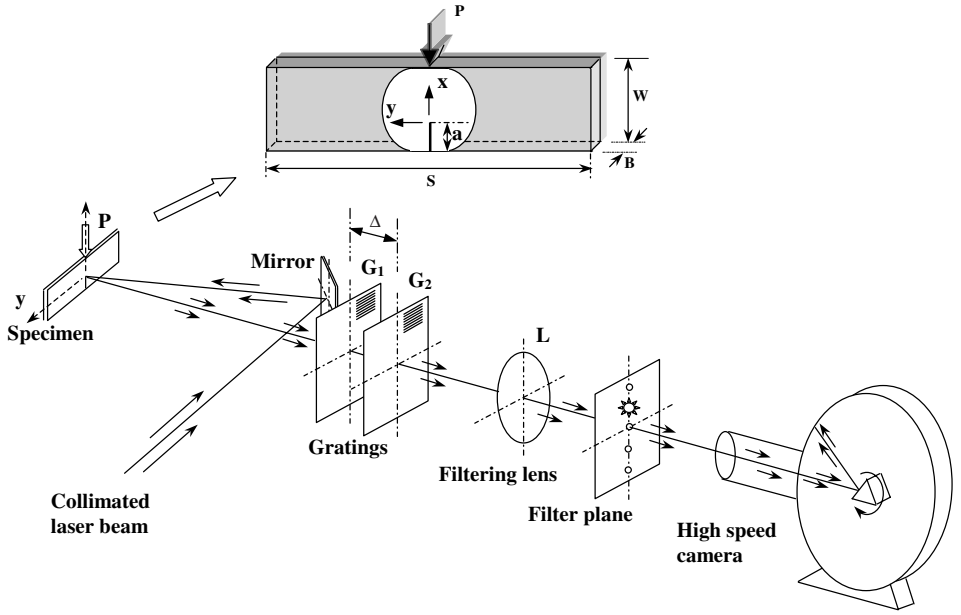

Fig. 2. Experimental set-up for reflection-mode CGS interferometry and high-speed imaging (specimen dimensions are $S = 152$ mm, $W = 42$ mm, $B = 8$ mm, $a = 10$ mm).

Interference fringes are the outcome of stress waves generated by the impact traveling back and forth across the sample, loading the notch tip to initiation. A crack subsequently propagates dynamically at speeds of up to 530 m/s in some specimens. Highly discernible fringes on the specimen surface around the impact point and crack tip are evident from the representative interferograms shown in Fig. 3. The first set of four fringes in Fig. 3(a) are for glass-filled epoxy with 11 μm particles, the next four (Fig. 3(b)) for 35 μm and the third set in Fig. 3(c) is for 203 μm. In each set, first two images are for pre-crack initiation instants while the next two are for post-initiation time instants. Impact point fringes (at the top of every image) develop and start accumulating as soon as the impactor contacts the specimen, while the crack tip fringes start appearing 35–40 μs after the initial impact. As stress waves reach the crack tip, tri-lobed fringes symmetric about the crack representing mode-I deformations start evolving around the crack tip. The second image in each set is a fringe pattern just before crack initiation. At initiation, a sudden release of energy results in stress waves emanating from the crack tip seen as a circular discontinuity in an otherwise continuous fringe pattern centered at the initial notch tip (third image of each set). After initiation, nearly stable crack growth ensues for about 40–60 μs. This is followed by a monotonic reduction in the size of lobes. These fringes represent contours of $\partial w/\partial x$ where w is the out-of-plane displacement. The resolution of the fringes is $\approx 0.015°$/fringe.

Fig. 4 shows the interference fringes for bimaterial (35 + 203 μm filler) with diffuse interface (Fig. 4(a)) and a bimaterial (35 − 203 μm filler) with discrete interface (Fig. 4(b)). (Note that the '+' sign represents the diffuse interface while '−' is used for its discrete counterpart.) In both sets first two images are from before crack initiation, while the next two are for the propagating crack. Fringe patterns for the diffuse interface are quite similar to those of 35 μm particle size fringes (Fig. 3(b)), but for a relatively smeared appearance due to the presence of larger size fillers. On the contrary in case of a discrete interface, the right half of these images show relatively less discernable fringes when compared to the left due to the presence of 203 μm particles. Emanating stress waves from the crack tip at initiation can be noticed in each set as well.

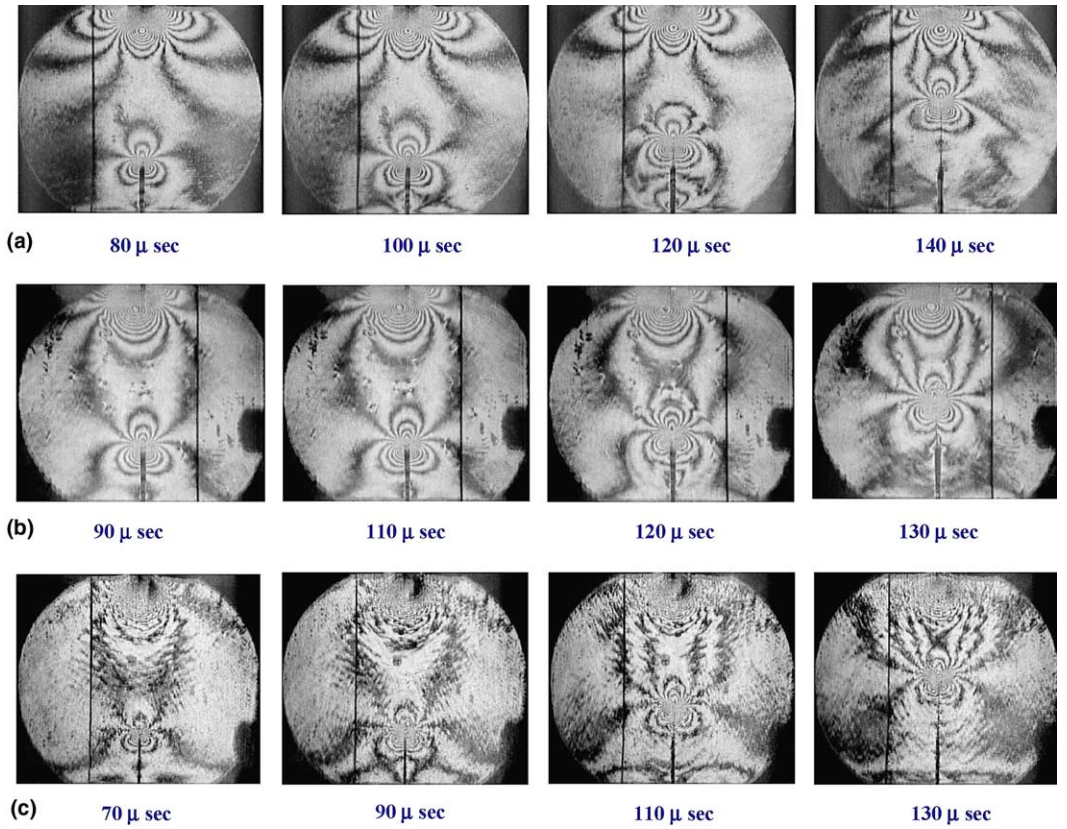

Fig. 3. Selected fringe pattern representing surface slope contours of $\partial w/\partial x$ for glass-filled epoxy specimens: (a) 11 μm particles, (b) 35 mm particles, and (c) 203 μm particles. Indicated time corresponds to the instant after impact.

3.1. Fringe analysis

Surface deformations are measured in terms of fringe order N, grating pitch p and grating separation distance Δ. In the present work, the principal direction of the gratings is chosen to be along the x-axis. Accordingly, the governing equation [30] can be written as

$$\frac{\partial w}{\partial x} = \frac{Np}{2\Delta} \approx -\frac{vB}{2E}\left[\frac{\partial(\sigma_x + \sigma_y)}{\partial x}\right], \quad N = 0, \pm 1, \pm 2, \pm 3, \ldots, \tag{2}$$

where w is expressed in terms of in-plane normal stresses using plane stress assumption and E is the elastic modulus, v is the Poisson's ratio and B is the undeformed thickness of the specimen. Williams [2] showed that the stress field singularity for an interface crack between two elastically dissimilar isotropic bimaterials to be of the form r^{λ}, where r is the distance from the crack tip and λ is $(-\frac{1}{2} + \mathrm{i}\epsilon)$ where $\epsilon = f(E_1, v_1, E_2, v_2)$ is the elastic mismatch parameter and $\mathrm{i} = \sqrt{-1}$. Subscripts 1 and 2 referred to the two halves of a bimaterial across the interface. The resulting dominant oscillatory stresses are of the form

$$\sigma \sim r^{-1/2}\begin{pmatrix}\sin \\ \cos\end{pmatrix}(\epsilon \log r). \tag{3}$$

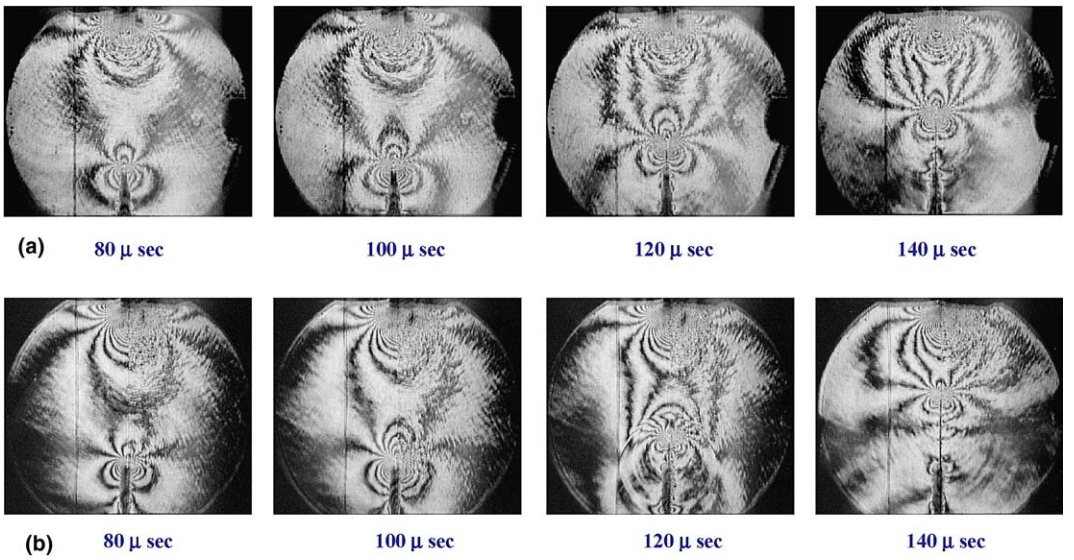

Fig. 4. Selected fringe pattern representing surface slope contours of $\partial w/\partial x$ for glass-filled epoxy bimaterial specimens: (a) (35 + 203 μm filler) diffuse interface, (b) (35 − 203 μm filler) discrete interface (left half contains 35 μm filler particles). Indicated time corresponds to the instant after impact.

The bimaterials in the current study are elastically similar macroscopically (see Table 1). That is, macro-scale elastic mismatch parameter $\epsilon = 0$ in Eq. (3). Hence, the crack tip field for homogeneous solids can be used in the analysis of fringes instead of the above-mentioned complex oscillatory singular stress field. Considering linear elastic asymptotic stress field in the vicinity of a steadily propagating mode-I crack [31], Eq. (2) can be written as

$$\frac{\partial w}{\partial x} = -\frac{vB}{2E} f(v) \sum_{n=1}^{\infty} \left[A_n \left(\frac{n}{2} - 1\right) r_l^{\left(\frac{n}{2}-2\right)} \cos\left(\frac{n}{2} - 2\right)\theta_1 \right] = \frac{Np}{2\Delta}, \tag{4}$$

where

$$\begin{aligned} f(v) &= \frac{(1+\alpha_s^2)(\alpha_l^2 - \alpha_s^2)}{4\alpha_l\alpha_s - (1+\alpha_s^2)^2}, \\ \theta_l &= \tan^{-1}(\alpha_l \tan\theta), \\ r_l &= r\cos\theta(1 + \alpha_l \tan^2\theta), \\ \alpha_{l:s} &= \sqrt{1 - (v/C_{l:s})^2}, \end{aligned} \tag{5}$$

r and θ are the polar coordinates defined at the instantaneous crack tip. Eq. (5) can also be used for analyzing pre-initiation interferograms as $f(v) \to 1$ as $v \to 0$. Overdeterministic least-squares analysis is performed on Eq. (4) and the resulting functional is minimized with respect to constants A_n. This results in a set of linear equations of the form

$$[Q]\{A\} = \{Z\}, \tag{6}$$

where $\{A\}$ is the vector of unknown constants A_n with $A_1 = K_1\sqrt{\frac{2}{\pi}}$, $[Q]$ is the matrix with its elements $Q_{ij} \equiv Q_{ij}(r, \theta, v, C_l, C_s)$ and $Z_i \equiv Z_i(r, \theta, N, E, v, B, v, C_l, C_s)$ is a known vector. The resulting set of linear equations are solved to get A_n.

3.2. Crack velocity and stress intensity factor

The framing rate of the high-speed imaging system is set to capture images every 5 μs after impact. The instantaneous crack length is measured by locating the crack tip from digitized images. From crack length histories, crack velocities are calculated using central difference method:

$$v_i = \left(\frac{\mathrm{d}a}{\mathrm{d}t}\right)_i = \frac{a_{i+1} - a_{i-1}}{t_{i+1} - t_{i-1}}. \tag{7}$$

The interferograms are used to extract fracture parameters by digitizing optical information around the crack tip to obtain fringe location, (r,θ), and fringe order, N, data. Using least-squares analysis described previously, mode-I dynamic stress intensity factors K_I are evaluated. The region of dominant 3-D effects in the vicinity of the crack tip ($r/B < 0.5$) is excluded from the analysis. Also, only the data behind the crack ($90° < \theta < 150°$) is considered since it has been demonstrated that triaxial effects are minimum in this region [30]. Since the measured data considered in the analysis comes from a region beyond $r/B = 0.5$, the inclusion of non-singular terms in the least-squares analysis is used to account for far-field stresses. It is found that by including first three terms of the asymptotic stress field, K_I can be evaluated accurately.

4. Results and discussion

Before considering the fracture behavior of glass-filled epoxy samples, dynamic fracture characteristics of the matrix material in the unfilled state is examined. Fig. 5(a) shows crack growth history for an unfilled/neat epoxy sample. The plot shows crack initiation at ~125 μs with an experimental accuracy of 5 μs. The instantaneous increase in velocities up to about 370 m/s can be noticed initially. The sudden release of energy from the initial notch tip results in rapid acceleration to about 2.5×10^7 m/s^2 and a maximum velocity ($v_{\max}$) of about 30% of the Rayleigh wave speed following crack initiation. A drop in the velocity following this initial acceleration to a steady state value (v_{ss}) of approximately 325 m/s can also be seen. The steady state crack growth region is followed by a continuous drop in velocity as the free surface and impact points are encountered by the propagating crack tip.

The stress intensity factor histories for unfilled epoxy is shown in Fig. 5(b). Stress intensity factor increases monotonically up to crack initiation. The rate of increase of stress intensity factor until crack initiation is $\sim 2.5 \times 10^4$ MPa $\sqrt{\mathrm{m}}$/s. The crack initiation toughness K_{Ii} is about 2.1 MPa $\sqrt{\mathrm{m}}$. Crack initiation is associated with a sudden drop in stress intensity factor which can be noticed in the figure. The maximum value of K_I just before the drop is identified as K_{Ii}. Further, instantaneous values of post-crack initiation stress intensity factors show an oscillatory behavior due to discrete wave reflections driving the crack forward. The post-crack initiation oscillations continue for about 45 μs. The average value of stress intensity factor for the period is identified as steady state fracture toughness ($K_{\mathrm{Iss}} \sim 1.5 \pm 0.1$ MPa $\sqrt{\mathrm{m}}$) of the material. The steady state behavior is followed by a monotonic drop in K_I until the specimen fracture is complete. The difference of time instants between crack initiation and the beginning of monotonic drop in stress intensity factor histories is quantified as the steady state duration (t_{ss}). The accuracy of fringe analysis beyond 180 μs is relatively low due to severe interaction between crack tip and impact point deformation fields.

4.1. Homogeneous glass-filled epoxy specimens

Next, dynamic fracture behavior of glass-filled monolithic epoxy specimens and role of filler-particle size on fracture parameters is presented. The crack velocity histories for specimens with glass-filled epoxy are

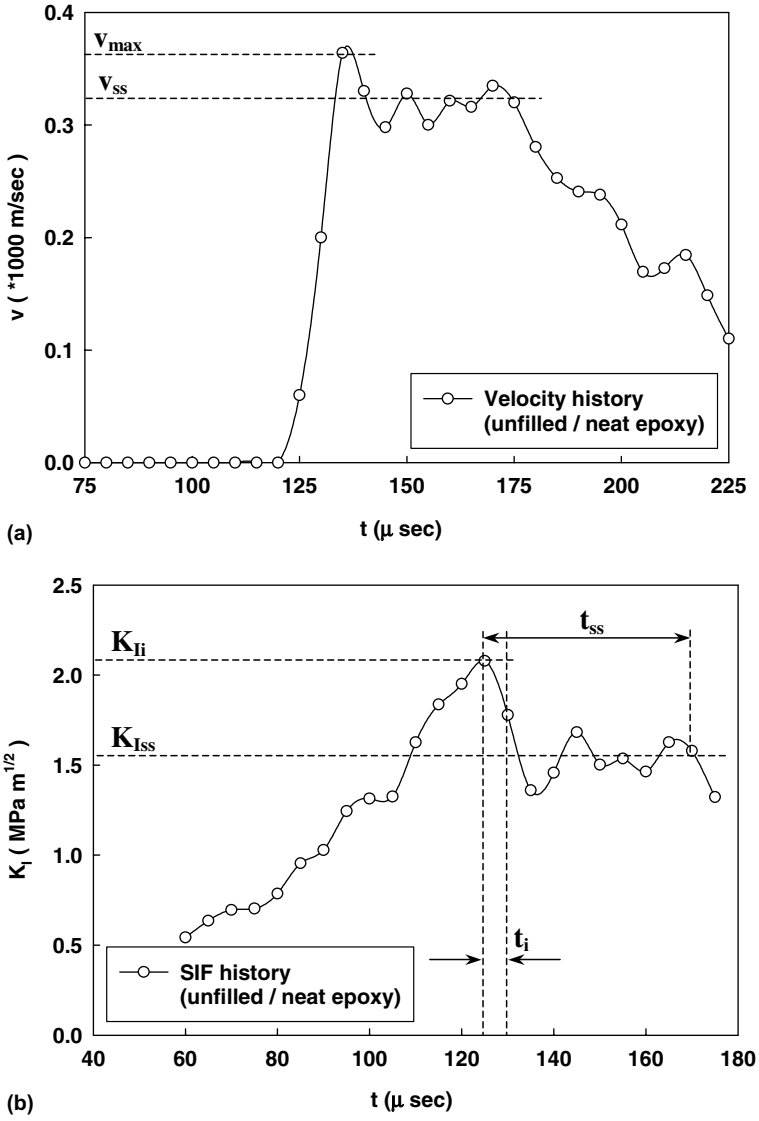

Fig. 5. Velocity and stress intensity factor histories for neat (unfilled) epoxy. Impact velocity 5.3 m/s. Subscripts "ss", "i" and "max" denote steady state, initiation and maximum values, respectively.

shown in Fig. 6(a). Results for only 11 μm, 35 μm and 203 μm sizes are shown in order to avoid data clutter. (The results for the other two particle sizes 7 μm and 71 μm are included in a table.) In each case, the crack velocity history shows a rapid increase in velocity at crack initiation reaching a maximum value $v_{\max}$ followed by a noticeable drop. Subsequently, the crack velocity is oscillatory about an average value, identified as steady state velocity, v_{ss}. These are similar to the unfilled epoxy results. The observations about crack initiation and growth are quantified in Table 2. The maximum crack velocity and acceleration at crack initiation increases as the particle size decreases. In the current study the maximum velocity ranges between ~325 m/s for the largest particles to ~500 m/s for the smallest in a monotonic fashion. The acceleration at

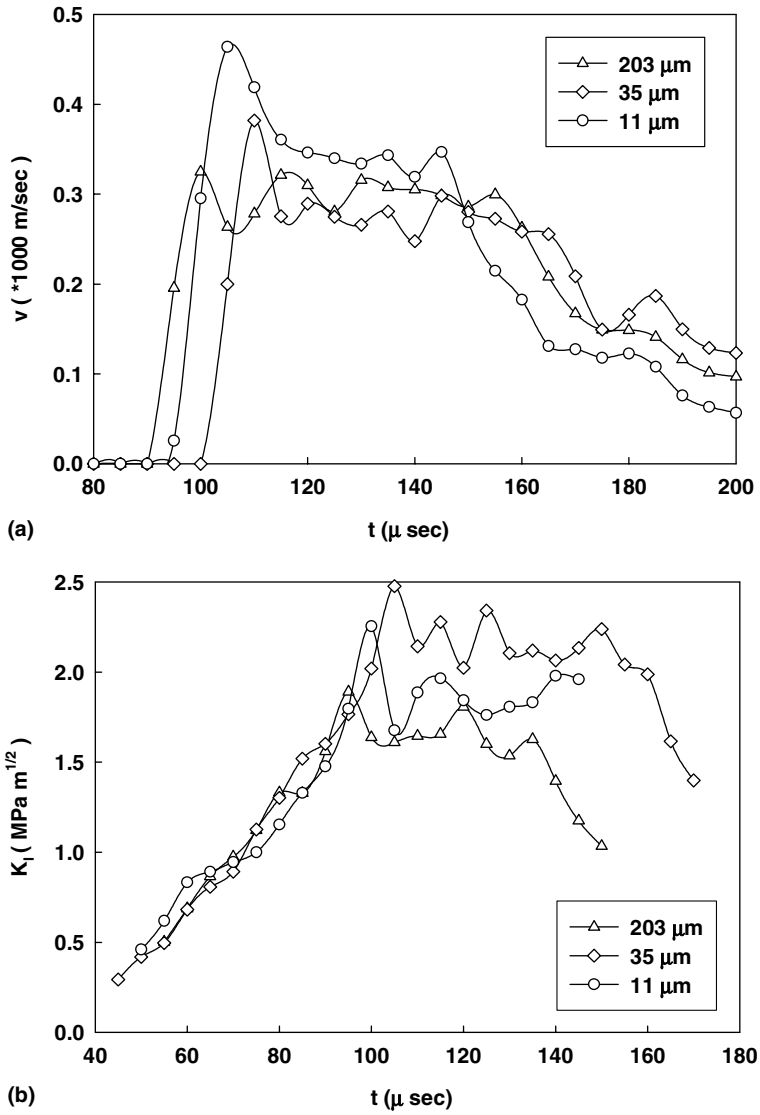

Fig. 6. Crack velocity histories (a) and stress intensity factor histories (b) for different glass-filled epoxy specimens.

Table 2
Crack growth parameters for glass-filled epoxy ($V_f = 0.1$) showing particle size effect on fracture parameters

Average particle diameter D (μm)	Crack initiation time t_i (μs)	Maximum crack velocity v_{max} (m/s)	Steady state crack velocity v_{ss} (m/s)	Steady state duration t_{ss} (μs)	Crack initiation toughness K_{Ii} (MPa $\sqrt{m}$)	Steady state fracture toughness K_{Iss} (MPa $\sqrt{m}$)
203	95–100	325	310	55	1.9 ± 0.05	1.7 ± 0.04
71	100–105	341	300	50	2.2 ± 0.08	1.9 ± 0.08
35	105–110	382	285	45	2.5 ± 0.05	2.3 ± 0.05
11	100–105	464	345	35	2.3 ± 0.10	2.0 ± 0.08
7	110–115	493	370	25	2.0 ± 0.15	1.9 ± 0.05
Epoxy	125–130	350	325	45	2.3 ± 0.15	1.5 ± 0.10

crack initiation is of the order of 10^7 m/s^2. As the particle size decreases, the duration of steady state crack growth, t_{ss}, decreases. That is, t_{ss} is the least for the smallest particle size and the longest for the largest particle size. It is noticed in these experiments that specimen fracture is complete at nearly the same time, ~260 μs, irrespective of the particle size. As the particle size decreases, maximum velocities increase. Since all the specimens take approximately the same time to fail completely, the duration of steady state growth t_{ss} decreases for smaller particles at the cost of higher maximum velocities. Table 2 shows minimum steady state velocity in case of 35 μm particles. Further increase or decrease in particle size results only in an increase in steady state velocity. This interesting velocity trend, which can be contrasted against steady state fracture toughness, is discussed later.

Stress intensity factor histories for glass-filled epoxy specimens (same particle sizes as in Fig. 6(a), for consistency) of various particle sizes are shown in Fig. 6(b). For each particle size, stress intensity factors monotonically increase until crack initiation. The average rate of increase in each case is $\frac{dK_I}{dt} \sim 32 \pm 3$ MPa $\sqrt{m}$/ms. Nearly the same crack tip loading rate attributed to similar macroscopic elastic characteristics (Table 1) irrespective of particle size. The crack initiation time varies from 95 μs to 115 μs for the considered particle sizes. In each case, crack initiation is followed by a small drop in K_I value followed by sustained oscillatory behavior about an average value. The K_{Ii} and K_{Iss} values for all particles are tabulated in Table 2. The steady state fracture toughness of unfilled epoxy is considered as a reference for further comparisons (see Table 2). Specimens with 35 μm particles show the highest value of K_{Iss}, which is approximately 65% higher when compared to the one for unfilled epoxy. With a decrease or an increase in particle sizes relative to 35 μm size, K_{Iss} shows a decreasing trend. Specimens with 11 μm particles show 40% and 7 μm particles show 34% higher fracture toughness, respectively, compared to the unfilled epoxy. From Table 2 it can be noticed that both 11 μm and 7 μm show similar stress intensity factor behaviors, with a relatively small difference in K_{Iss} suggesting possible saturation of fracture toughness as particle size decreases. This is similar to the decreasing trend in fracture toughness for particle sizes below 42 μm reported in Refs. [28,29] for the silica-filled epoxy. Similar effects have been noticed when particle size is increased beyond 35 μm. Specimens with 71 μm and 203 μm particles show approximately 37% and 18% increase in fracture toughness compared to unfilled epoxy, which is successively lower compared to the ones with

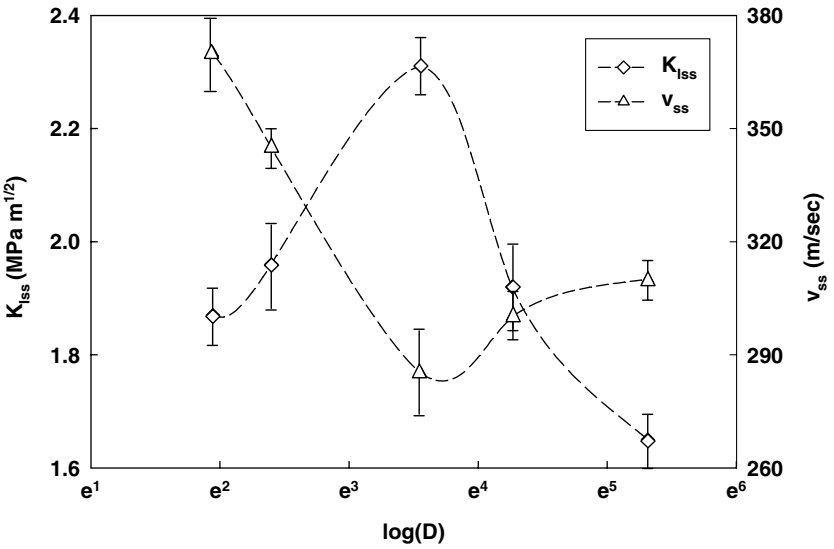

Fig. 7. Variation of steady state velocity and fracture toughness with particle size in glass-filled epoxy with weakly bonded fillers.

35 μm particles. Fig. 7 summarizes particle size effect on K_{Iss} in case of glass-filled epoxy at 10% volume fraction. Evidently, there is a discernible optimum particle size at which fracture toughness is maximum for the selected volume fraction. As the particle size increases or decreases relative to this optimum value, the steady state fracture toughness decreases. Quite interestingly the optimum particle size for maximum steady state fracture toughness also corresponds to the minimum steady state velocity. With a decrease or an increase in particle size relative to the optimum value, monotonic decrease in fracture toughness is associated with an increase in the steady state velocity. That is, an inverse relationship between steady state velocity and fracture toughness is evident (see Fig. 7). Error bars shown in figure are based on multiple experiments and experimental repeatability (see, Appendix A). That is, the reported behavior is measurably outside the range of experimental errors. From Table 2 it can also be noticed that K_{Ii} trends are similar to that of K_{Iss}. The trends again reveal the optimum particle size to be 35 μm. Comparison shows that K_{Ii} is higher by 35%, 56%, 77%, 61% and 41% for 203 μm, 71 μm, 35 μm, 11 μm and 7 μm, respectively, compared to the unfilled epoxy.

4.1.1. Fractography

Scanning electron microscopy (SEM) is used for examining fracture surfaces and seek qualitative explanation for the non-monotonic K_{Iss} values with filler particle size seen in Fig. 7. Approximately 1.5–2 mm thin strip of fractured surface with cross-sectional area 42 mm × 8 mm is stripped out and deposited with a thin layer of gold. Various locations in the steady state crack growth region (mid one-third region) using SEM are examined. Fig. 8 shows micrographs of a few representative fractured surfaces. The images in Fig. 8(a)–(c) are for 203 μm, 35 μm and 11 μm particle sizes respectively. *It is evident from the micrographs that agglomeration effects are essentially non-existent in these cases and can be ruled out as the cause of the observed microstructural effects on crack growth.* Highly textured surface for the 35 μm particles suggest higher energy dissipation and hence higher fracture toughness compared to 203 μm particles. It is noticed that filler particles are unbroken and the crack always travels through the matrix material. Micrographs show inter-particle cleavage fracture with either particle or particle foot-prints left behind on the surface. Clearly the matrix surrounding the filler particles is separated from the weakly bonded filler-particles as the crack front encounters filler–matrix interface. In this process the crack tip gets blunted locally, wherever it meets the filler phase, lowering the stress intensification at the crack tip. This requires additional energy to overcome the local blunting effect, so that the crack can re-initiate and propagate further. Intermittent stalling of a growing crack correlates with lower average crack velocity and higher fracture toughness. The

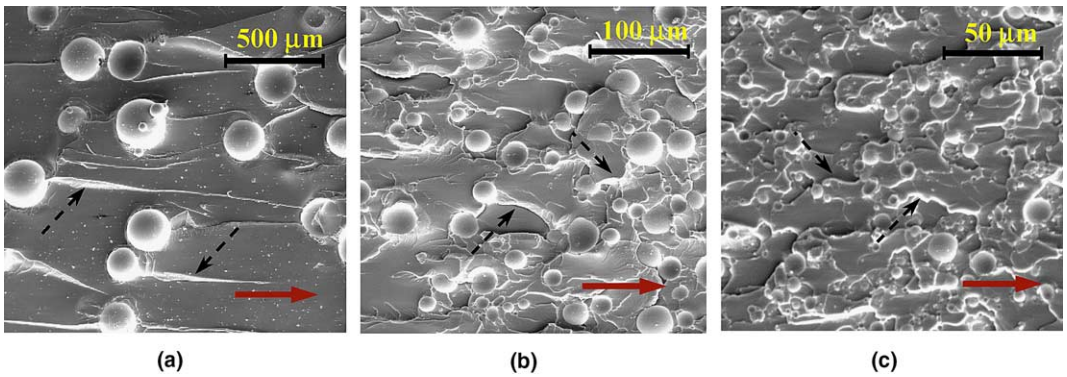

Fig. 8. SEM micrographs: (a) 203 μm particles, (b) 35 μm particles, (c) 11 μm particles. Solid arrow shows crack propagation direction and broken arrow shows "Tail lines".

inverse relationship between crack velocity and fracture toughness due to blunting effect can be noticed in Figs. 7 and 10. Neighboring filler particles at different elevations with respect to crack surface produce twisting of a propagating crack front [32]. When the angle-of-twist reaches its limiting value, "tail lines" emerge from the particle sites, creating extra new surface in matrix material. Tail lines emerging from the particles/cavities or within matrix material can be seen in micrographs, which show direction of crack propagation. These lines are also indicative of the magnitude of surface tortuosity and crack front twisting during fracture. Clearly, tail lines/crack twisting is another cause of additional energy dissipation and hence of higher fracture toughness. However, it should be noted that the limiting angle-of-twist depends on particle size, filler–matrix adhesion strength, elastic and failure properties of filler and matrix, etc. In summary, at least two mechanisms, localized crack tip blunting and crack front twistings, are evident from the micrographs. The combined effect and the competition between these two mechanisms are likely behind the non-monotonic K_{Iss} variation as seen in Fig. 7.

Non-monotonic bell shaped variation in K_{Iss} with an optimum particle size for maximum fracture toughness under dynamic loading could raise the question, is this fracture behavior loading rate and volume fraction dependent? Addressing the latter parameter is beyond the scope of the present work but the former can be addressed in a limited sense by measuring values of critical stress intensity factors of glass-filled epoxy sheets under quasi-static loading conditions and comparing the results with the dynamic observations. Accordingly, experiments were performed on homogeneous compositions using quasi-static loading prior to choosing particle sizes for bimaterial specimens. These experimental results are reported in Appendix B for completeness. The investigation shows significant differences in static crack initiation fracture toughness values for various particle sizes when compared to the dynamic steady state ones. However, similar fracture toughness trends for the two different loading conditions seem to exist.

4.2. Glass-filled epoxy bimaterials

4.2.1. Diffuse interface

From the observed particle size effects discussed in the previous section, (Fig. 7 and Table 2), maximum and minimum fracture toughness correspond to 35 μm and 203 μm particles, respectively. To examine the effect of a diffuse interface with mixed filler particles on fracture parameters, these two particle sizes were chosen due to a relatively large difference in fracture toughness values in monolithic configuration. Fig. 9(a) shows the comparison of velocity history for mixed fillers (35 μm + 203 μm) along with the ones for individual 35 μm and 203 μm particle sizes. Similar to single size filler particles, mixed fillers also show a rapid increase in velocity at initiation until it reaches a maximum followed by a drop and a subsequent oscillatory behavior about an average. The steady state velocity is similar to those for 35 μm and 203 μm particle sizes and approximately bounded by those obtained in the monolithic configuration.

Fig. 9(b) shows comparison of stress intensity factor histories for diffuse interface with mixed fillers (35 μm + 203 μm) with those for individual particle sizes. All particle sizes including the mixed ones show a monotonic increase in stress intensity factor until crack initiation. The average rate of increase in mixed fillers is $\sim 3.4 \times 10^4$ MPa $\sqrt{\mathrm{m}}$/s, which is close to the ones with 35 μm and 203 μm filler particles. Similar crack tip loading rate in each case can again be attributed to similar macroscopic elastic properties (see Table 1). The crack initiates between 105 μs and 110 μs for the diffuse interface. Both t_i and K_{Ii} for this case are very close to the respective values for 35 μm particles. Similar to 35 μm and 203 μm fillers crack growth along diffuse interface shows a drop in stress intensity factor at initiation followed by an oscillatory behavior. Some of the observations about velocity and stress intensity factor are quantified in Table 3. The steady state fracture toughness value for the diffuse interface ($\sim$2.0 MPa $\sqrt{\mathrm{m}}$) is between the respective values for monolithic samples with 35 μm and 203 μm particles. Further, K_{Iss} for the diffuse interface is about 33% higher than that of the unfilled epoxy.

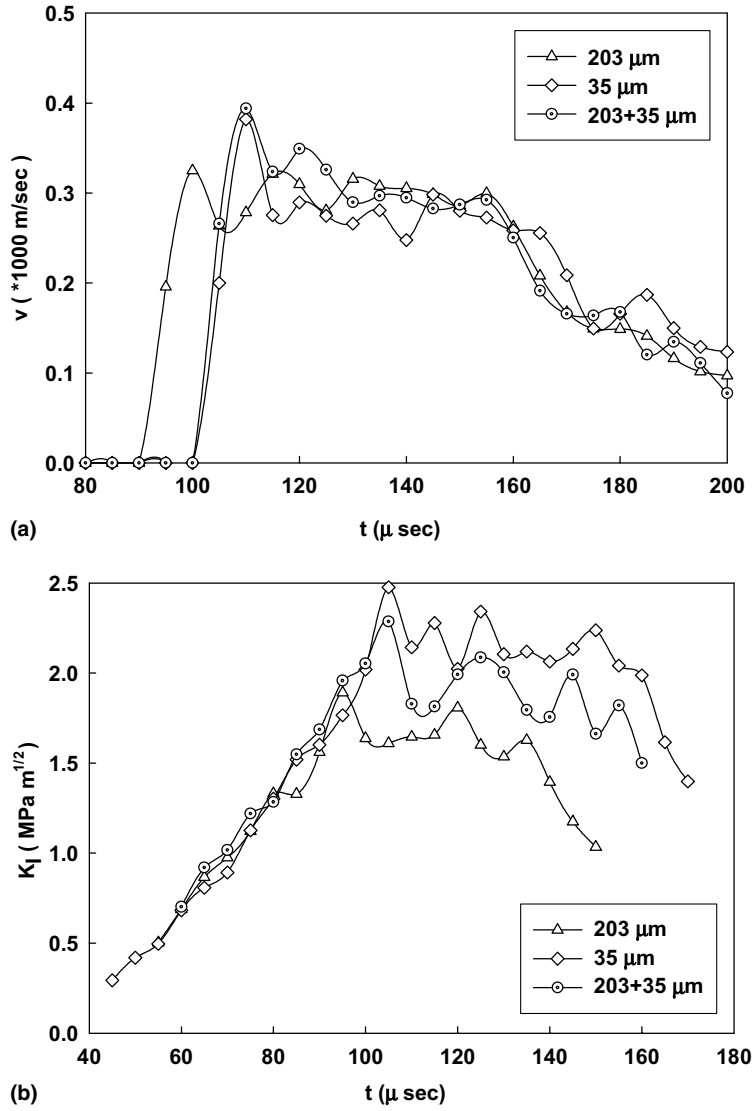

Fig. 9. Crack velocity history (a) and stress intensity factor history (b) in 203 + 35 μm bimaterial with diffuse interface (total filler $V_f = 10\%$). For comparison, corresponding histories of monolithic specimens are also shown.

Table 3
Crack growth parameters for glass-filled epoxy with single size filler particles and bimaterial mixtures with diffuse interface ($V_f = 0.1$)

Average particle diameter D (μm)	Crack initiation time t_i (μs)	Maximum crack velocity v_{max} (m/s)	Steady state crack velocity v_{ss} (m/s)	Steady state duration t_{ss} (μs)	Crack initiation toughness K_{Ii} (MPa $\sqrt{m}$)	Steady state fracture toughness K_{Iss} (MPa $\sqrt{m}$)
35	105–110	382	285	45	2.5 ± 0.05	2.3 ± 0.05
35 + 203	105–110	394	295	50	2.3 ± 0.10	2.0 ± 0.10
203	95–100	325	310	55	1.9 ± 0.05	1.7 ± 0.04
11 + 203	100–105	408	335	40	2.2 ± 0.08	1.8 ± 0.05
11	100–105	464	345	35	2.3 ± 0.10	2.0 ± 0.08

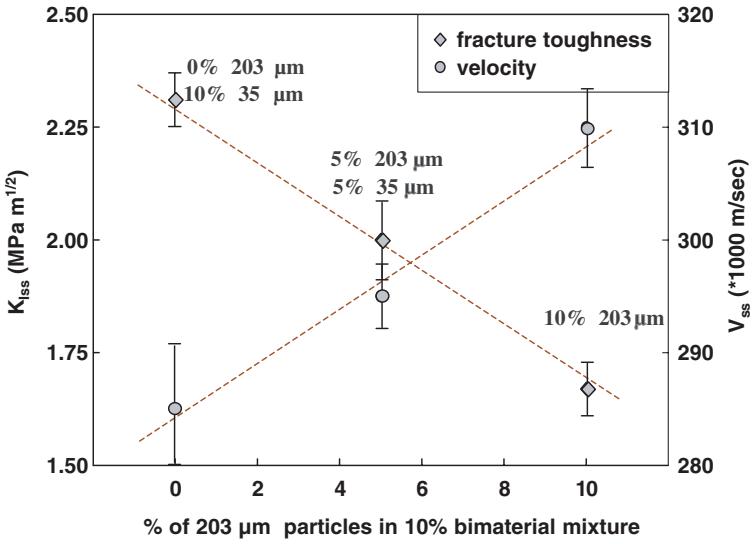

Fig. 10. Steady state fracture toughness and steady state velocity variation with constituent filler percentage in 10% glass-filled (bimaterial with diffuse interface) epoxy specimens.

Fig. 10 summarizes the effect of diffuse interface with mixed particle on steady state fracture toughness and steady state velocity. Horizontal axis represents the volume fraction of 203 μm particles in the mixture. The two vertical axes represent steady state fracture toughness and velocity, respectively. The plot shows nearly a linear variation of K_{Iss} with V_f of the constituent particle sizes. Variation in v_{ss} with constituent particle volume fraction is not so discernible as K_{Iss} due to a relatively small velocity range. However, a monotonic variation of v_{ss} with constituent particle V_f is observable. Further, considering only the average of velocities, both v_{ss} and K_{Iss} plots show nearly linear variations with V_f of the constituent particle sizes but with opposite slopes, respectively. This is consistent with the inverse relationship between steady state velocity and fracture toughness seen previously while studying particle size effect.

To further confirm the influence of particle sizes in a diffuse interface on velocity and fracture toughness, experiments were also performed on another diffuse interface consisting of 203 and 11 μm particles at 5% V_f each. Table 3 shows the resultant steady state velocity and stress intensity factors. Similar to 203 + 35 μm diffuse interface results, v_{ss} and K_{Iss} values for 203 + 11 μm bimaterial fall in between the respective values for the monolithic specimen with the respective reinforcement sizes. Details are avoided here for brevity. Both velocity and fracture toughness values vary monotonically with constituent volume fractions with opposite slopes (see Table 3). Steady state velocity and fracture toughness relationship is also monotonic with a negative slope as shown in case of 203 μm+35 μm mixture.

4.2.2. Discrete interfaces

Discrete bimaterial interface with two halves and made of glass-filled epoxy reinforced with 203 μm and 35 μm particles is discussed next. Fig. 11(a) shows a comparison of crack velocity history of discrete interface with those for homogeneous specimens with the same constituent fillers at 10% V_f. The velocity rises rapidly following initiation with an estimated acceleration of the order $\sim 10^7$ m/s^2, similar to the homogeneous counterparts. Again, discrete interfacial crack growth also shows a noticeable drop following maximum velocity v_{max} and a steady oscillatory behavior about an average v_{ss}. From Table 4 it can be noticed

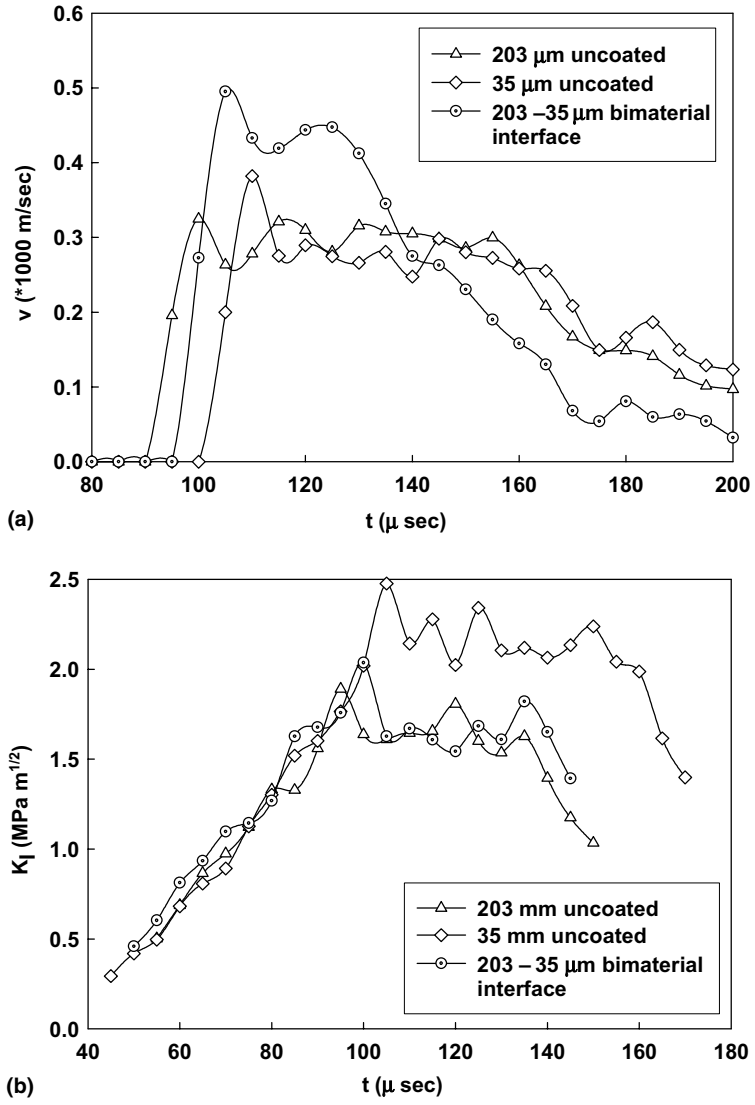

Fig. 11. Velocity history (a) and stress intensity factor history (b), for 203 − 35 μm discrete bimaterial interface and the corresponding monolithic specimens with 10% filler V_f.

Table 4
Crack growth parameters for glass-filled epoxy with a single size filler and bimaterial with discrete interface ($V_f = 0.1$)

Average particle diameter D (μm)	Crack initiation time t_i (μs)	Maximum crack velocity v_{max} (m/s)	Steady state crack velocity v_{ss} (m/s)	Steady state duration t_{ss} (μs)	Crack initiation toughness K_{Ii} (MPa $\sqrt{m}$)	Steady state fracture toughness K_{Iss} (MPa $\sqrt{m}$)
35	105–110	382	285	45	2.5 ± 0.05	2.3 ± 0.05
3 − 203	100–105	495	430	40	2.0 ± 0.10	1.7 ± 0.08
203	95–100	325	310	55	1.9 ± 0.05	1.7 ± 0.04
203 − 11	100–105	405	340	30	2.1 ± 0.15	1.7 ± 0.10
11	100–105	464	345	35	2.3 ± 0.10	2.0 ± 0.08

that maximum and steady state velocities are significantly higher for the bimaterial when compared to its homogeneous counterparts involving the same size fillers. Further, a comparatively smaller steady state crack growth region is followed by a monotonic drop in crack velocity until the completion of specimen fracture.

The stress intensity factor history for the discrete interface also shows a monotonic increase in K_I until crack initiation (see Fig. 11(b)). The average crack tip loading rate ($\sim$32 MPa $\sqrt{m}$/ms) is same as those of its homogeneous counterpart. Crack initiation is followed by a comparatively larger drop in K_I and an oscillatory behavior about an average value, K_{Iss}. The figure shows the oscillatory behavior of the bimaterial with discrete interface to be closer to that of the homogeneous specimen with 203 μm filler. A steady state fracture toughness value K_{Iss} of $\sim$1.7 MPa $\sqrt{m}$, can be seen and the value is approximately same as the one for homogeneous specimen filled with only 203 μm particles. Similar to its homogeneous counterparts, oscillatory behavior in the bimaterial is followed by a monotonic drop in K_I until complete fracture of the specimen occurs.

Discrete bimaterial interface made of filled epoxy with 203 μm and 11 μm halves is also studied. Crack initiation and growth parameters are quantified in Table 4. Similar to 203 −35 μm discrete interface, 203–11 μm bimaterial shows a steady state behavior to be very close to the weaker (lower K_{Iss}) material namely the sample with 203 μm fillers, having a steady state fracture toughness $K_{Iss} \approx 1.7$ MPa $\sqrt{m}$.

4.2.3. Fractography

SEM micrographs of the fracture surfaces is used to provide supplementary explanation for the observed fracture behaviors in the two types of bimaterials relative to the homogeneous counterparts. Fig. 12(a) shows fractured surface for 35 + 203 μm diffuse interface. A homogeneous distribution of larger as well as smaller particle/particle foot prints are obvious from the micrographs. It can also be noted that diffuse interface has higher roughness when compared to the homogeneous specimen with 203 μm diameter particle (Fig. 8(a)), while it shows lower roughness relative to the one with 35 μm particles (Fig. 8(b)). This commensurates well with the optical measurements namely, a steady state fracture toughness for interface

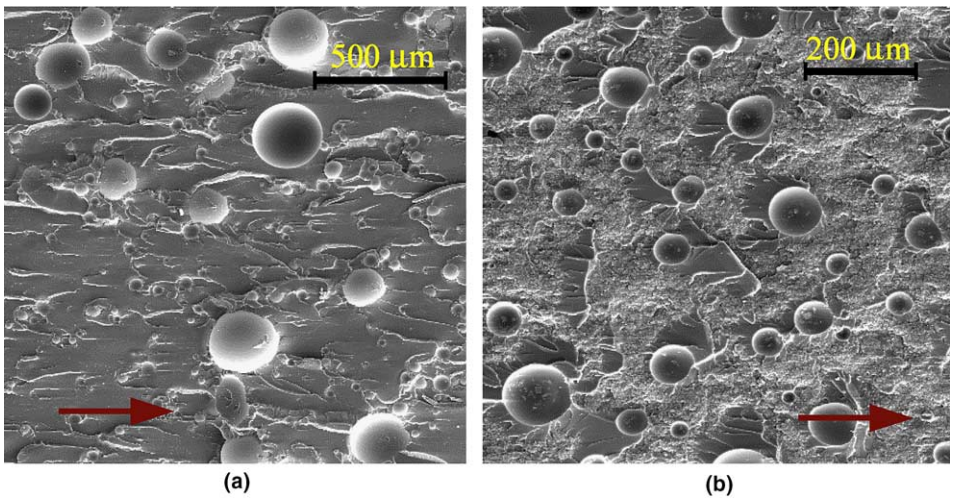

Fig. 12. SEM micrographs of fractured surfaces: (a, b) show the 35 + 203 μm diffuse interface and 35 − 203 μm discrete interface, respectively.

crack is bounded by those for 203 μm and 35 μm particle sizes. Tail lines indicating crack propagation direction can again be seen in case of diffuse interface.

Fig. 12(b) shows fractured surface of 35 − 203μm discrete interface. The fracture surface is qualitatively distinct from the ones shown in Fig. 8(a) and (b) for monolithic materials with 35 μm and 203 μm particles alone. Unlike the smooth cleavage fracture in monolithic materials, rugged surface in between particle foot-prints can be noticed in discrete interface fracture surface. The observed particle foot-prints are invariably larger than 35 μm diameter. This suggests that the crack has traveled primarily through 203 μm particle sided half of the bimaterial. No sign of smaller particles/particle foot-prints further strengthens the observed behavior. Different sized particle foot-prints are an indication of crack–particle interaction at various latitudes of a particle. Crack growth through the weaker material can also be concluded from experimental results, where the fracture toughness of discrete interface is found to be very close to the epoxy filled with 203 μm particles.

5. Conclusions

Interfacial fracture behavior of particulate bimaterials with diffuse and discrete microstructures is studied experimentally. Epoxy sheets reinforced with glass particles of distinctly different sizes are used in the study. First, the influence of filler particle size on dynamic fracture behavior of homogeneous particulate composite specimens is studied. Solid glass particles from 7 μm to 203 μm in mean diameter are used to prepare macroscopically homogeneous test specimens at 10% filler volume fraction. The reflection CGS method and high-speed photography are used to measure crack tip fields. The fracture parameters are evaluated using the interferograms. The particle size effect on fracture behavior is summarized as follows:

- Particle size does not show discernable influence on elastic properties at 10% filler volume fraction.
- Glass-filled epoxies show higher steady state fracture toughness (K_{Iss}) compared to unfilled epoxy.
- Measurable particle size effect on steady state velocity (v_{ss}) and fracture toughness (K_{Iss}) is noticed. There is a distinct optimum particles size (35 μm in the current study) at which fracture toughness is maximum. This is also associated with minimum crack velocity (v_{ss}). K_{Iss} and v_{ss} vary monotonically on either side relative to the optimum particle size. Steady state velocity, v_{ss} shows an inverse relationship with K_{Iss}.
- Crack front twisting and localized crack tip blunting are dominant but competing toughening mechanisms for the observed particle size effect.

In the second phase of the study, discrete and diffuse bimaterials are investigated. The particle sizes selected provided the largest possible mismatch in fracture toughness, based on the first part of the study on monolithic compositions. A step change in particle size is used to create discrete interfaces. In case of a diffuse interface, two distinctly different particle sizes are equally intermixed. Some of the observations are summarized below:

- Both crack velocity (v_{ss}) and fracture toughness (K_{Iss}) values for diffuse bimaterials at 10% V_f are bounded by the respective values of homogeneous monolithic particulate composite containing a single particle size.
- Both v_{ss} and K_{Iss} seems to vary linearly with constituent particle volume fraction in diffuse bimaterials. Steady state fracture toughness K_{Iss} shows negative linear variation with v_{ss}.
- Both maximum and steady state velocities for discrete bimaterial interfaces are significantly higher than monolithic counterparts.
- Steady state fracture toughness for bimaterial with discrete interface is same as the one for the weaker material of its two halves

Acknowledgments

The authors gratefully acknowledge the support of the research through grants from NSF (CMS-9912066) and ARO (W911NF-04-1-0257). Authors would also like to thank Mr. Chris Smith, Technical Manager at Potters Industries, Inc., for his enthusiastic support of the research and for providing glass microspheres used in this investigation.

Appendix A

While investigating particle size effect on dynamic fracture behavior of glass-filled epoxy specimens multiple experiments were performed for each particle size. Atleast two repeatable dynamic crack growth results have been considered in determining steady state velocity and steady state fracture toughness. As an example, Fig. 13 shows stress intensity factor histories for two 35 μm glass-filled epoxy specimens. Pre-initiation stress intensity factor histories essentially overlap. In each case the stress intensity factor increases monotonically up to crack initiation with a rate of increase $\sim 34 \times 10^3$ MPa $\sqrt{\text{m}}$/s. In both the experiments the crack initiated at ~105 μs and crack initiation toughness K_{Ii} is ~2.5 MPa $\sqrt{\text{m}}$. The crack initiation is followed by a noticeable drop and an oscillatory but steady state zone for ~50 μs. Post-crack initiation fracture behaviors are also nearly similar for both the specimens and steady state fracture toughness K_{Iss} is $\sim 2.3 \pm 0.05$ MPa $\sqrt{\text{m}}$. The steady state behavior is followed by a monotonic drop in K_{I} until the specimen fracture is complete. Similar crack velocity histories are also noticed in both specimens but are not presented here for brevity. Such similarities in pre- and post-initiation behavior for crack tip velocity and stress intensity factor histories in multiple specimens suggest the robustness and repeatability of the experiments and the method employed in this study.

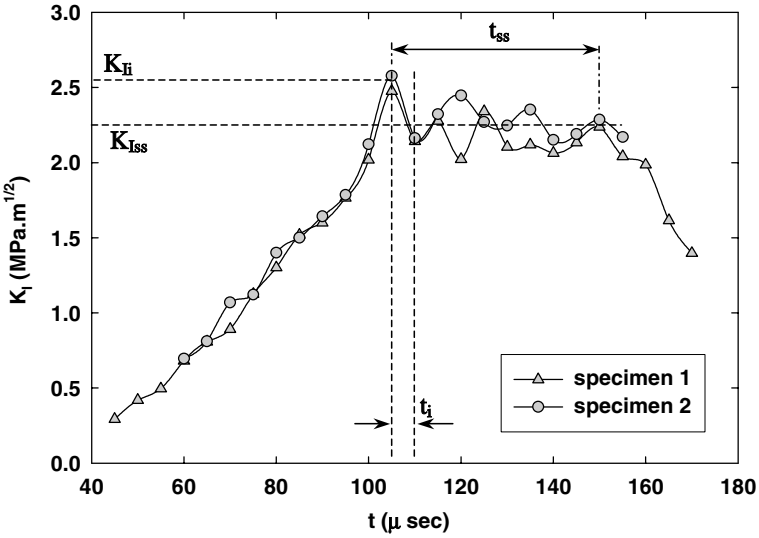

Fig. 13. Stress intensity factor histories for two identical specimens with 35 μm filler particles demonstrating repeatability of experimental measurements.

Appendix B

The investigation of filler particle size on dynamic fracture toughness for monolithic material is described earlier. The 10% V_f glass-filled epoxy shows non-monotonic variation of K_{Iss} (see, Fig. 7) and K_{Ii} (see, Table 2) with particle size under dynamic loading conditions. Experiments also suggest an optimum particle size (35 μm in this study) for maximum fracture toughness. An obvious question that arises from this result is, is the particle size effect on fracture behavior loading rate dependent? This led authors to perform experiments under quasi-static loading conditions and retrieve the fracture parameters for different particle sizes prior to choosing the two particle sizes with maximum fracture toughness mismatch for preparing bimaterial specimens.

The monolithic sheets were first prepared from 10% V_f glass-filled epoxy mixture as described in Section 2.1. An edge notch of 5 mm nominal length was cut into the machined samples of the dimensions 90 mm × 30 mm × 8 mm. Further a sharp crack of length 8–12 mm was grown by forcing a wedge into the pre-cut notch and 'pop' the crack tip and arrest it in a controlled fashion. Thus prepared single edge notched bend (SENB) specimens were loaded in displacement control mode (0.25 mm/min) in a symmetric three point bending configuration using an INSTRON 4465 testing machine. The load at crack initiation was recorded and the crack initiation toughness, K_{Ic} was calculated using the measured fracture load and the specimen geometry [33].

The experiments involved 3–5 samples for each filler particle sizes. The static crack initiation toughness (K_{Ic}) values for various particle sizes are tabulated in Table 5. For comparison purposes the dynamic fracture parameters (K_{Ii} and K_{Iss}) for respective particle sizes are also presented. Fig. 14 shows the variation of K_{Ic} and K_{Iss} with filler particle size. From the plot it can be seen that, similar to K_{Iss} variation, the variation of K_{Ic} is non-monotonic with the particle size. The optimum particle size among the several others considered for maximum fracture toughness again turns out to be 35 μm. With a decrease or an increase in particle size relative to this optimum size, fracture toughness decreases. Similar trends in fracture toughness variation for both quasi-static and dynamic loading cases suggest that the fracture toughness variation with particle size is independent of the loading conditions. However, from the plots it can be noticed that the fracture toughness values between static and dynamic cases differ from each other for respective particle sizes. The difference is quite significant for 35 μm particles, where the fracture toughness value for static case is ~40% higher when compared to the dynamic case. The static fracture toughness values are higher when compared to the dynamic case when filler particles are of sizes close to the optimum particle size. Particle sizes 20 μm, 35 μm and 85 μm show higher static fracture toughness for 10% V_f. Also, the static

Table 5
Crack growth parameters for glass-filled epoxy ($V_f = 0.1$) showing loading rate dependence as well as particle size effect on fracture parameters

Average particle diameter D (μm)	Static crack initiation toughness K_{Ic} (MPa $\sqrt{m}$)	Dynamic crack initiation toughness K_{Ii} (MPa $\sqrt{m}$)	Dynamic steady state fracture toughness K_{Iss} (MPa $\sqrt{m}$)
203	1.28 ± 0.15	1.9 ± 0.05	1.7 ± 0.04
85	1.65 ± 0.10	–	–
71	1.98 ± 0.05	2.2 ± 0.08	1.9 ± 0.08
35	3.36 ± 0.25	2.5 ± 0.05	2.3 ± 0.05
20	2.37 ± 0.10	–	–
11	1.69 ± 0.00	2.3 ± 0.10	2.0 ± 0.08
7	1.55 ± 0.05	2.0 ± 0.15	1.9 ± 0.05
Epoxy	1.09 ± 0.05	2.3 ± 0.15	1.5 ± 0.10

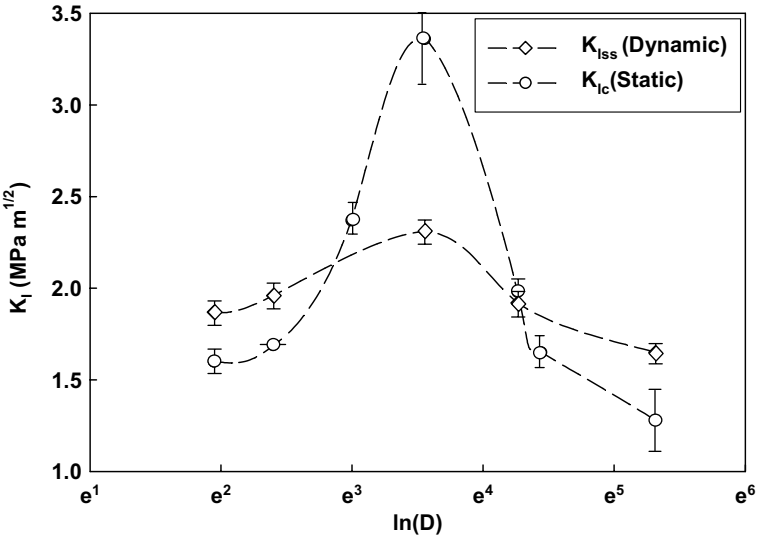

Fig. 14. Role of loading rate on fracture parameters of glass-filled epoxy ($V_f = 10\%$) with different filler particle sizes.

fracture toughness values appear to be saturating as particle size is further increased/decreased relative to the optimum particle size, similar to the dynamic case.

References

[1] Hutchinson JW, Mear ME, Rice JR. Crack paralleling an interface between dissimilar materials. Trans ASME 1987;54:828–31.
[2] Williams ML. The stresses around a fault or crack in dissimilar media. Bul Seismol Soc Amer 1959;49(2):199–203.
[3] Rice JR. Elastic fracture mechanics concepts for interfacial cracks. J Appl Mech—Trans ASME 1988;55:98–103.
[4] Shih CF. Cracks on bimaterial interfaces: elasticity and plasticity aspects. Mater Sci Eng 1991;A143:77–90.
[5] Charalambides PG, Lund J, Evans AG, McMeeking RM. A test specimen for determining the fracture resistance of bimaterial interfaces. J Appl Mech 1989;56:77–82.
[6] Leichti KM, Chai YS. Biaxial loading experiments for determining interfacial fracture toughness. J Appl Mech—Trans ASME 1991;58:680–7.
[7] Xu L, Tippur HV. Fracture parameters for interfacial cracks: an experimental-finite element study of crack tip fields and crack initiation toughness. Int J Fract 1995;71:345–63.
[8] Tippur HV, Rosakis AJ. Quasi-static and dynamic crack growth along bimaterial interfaces: a note on crack-tip field measurements using coherent gradient sensing. Exp Mech 1991;33:243–52.
[9] Yang W, Suo Z, Shih CF. Mechanics of dynamic debonding. Proc Royal Soc Lond 1991;A433:679–97.
[10] Liu C, Lambros J, Rosakis AJ. Highly transient elastodynamic crack growth in a bimaterial interface: higher order asymptotic analysis and optical measurements. J Mech Phys Solids 1993;41(12):1887–954.
[11] Xu XP, Needleman A. Numerical simulations of dynamic crack growth along an interface. Int J Fract 1996;74:289–324.
[12] Lo CY, Nakamura T, Kushner A. Computational analysis of dynamic crack propagation along a bimaterial interface. Int J Solids Struct 1994;31(2):145–68.
[13] Singh RP, Shukla A. Subsonic and intersonic crack growth along a bimaterial interface. J Appl Mech—Trans ASME 1996;63(4):919–24.
[14] Erdogan F. Fracture mechanics of functionally graded materials. Compos Eng 1995;5(7):753–70.
[15] Butcher RJ, Rousseau CE, Tippur HV. A functionally graded particulate composite: preparation, measurements and failure analysis. Acta Mater 1999;47(1):259–68.
[16] Marur PR, Tippur HV. Dynamic response of bimaterial and graded interface cracks under impact loading. Int J Fract 2000;103:95–109.
[17] Khor KA, Dong ZL, Gu YW. Plasma sprayed functionally graded thermal barrier coatings. Mater Lett 1999;38:437–44.

[18] Jung YG, Paik U, Choi C. Influence of the particle size and phase type of zirconia on the fabrication and residual stress of zirconia/stainless-steel 304 functionally graded material. J Mater Sci 1999;34:5407–16.
[19] Fukui Y, Takashima K, Ponton CB. Measurement of Young's modulus and internal friction of an in situ Al–Al_3Ni functionally gradient material. J Mater Sci 1994;29:2281–8.
[20] Marur PR, Tippur HV. Numerical analysis of crack-tip fields in functionally graded materials with a crack normal to the elastic gradient. Int J Solids Struct 2000;37:5353–70.
[21] Rousseau CE, Tippur HV. Influence of elastic gradient profiles on dynamically loaded functionally graded materials: cracks along the gradient. Int J Solids Struct 2001;38:7839–56.
[22] Tandon S, Faber KT. Effects of loading rate on the fracture of cementitious materials. Cem Concr Res 1999;29:397–406.
[23] Issa AMo, Issa AMa, Islam MS, Chudnovsky A. Fractal dimension-a measure of fracture roughness and toughness of concrete. Eng Fract Mech 2003;70:125–37.
[24] Abell AB, Lange DA. Fracture mechanics modeling using images of fracture surfaces. Int J Solids Struct 1998;35:4025–33.
[25] Spanoudakis J, Young RJ. Crack propagation in a glass particle-filled epoxy resin. Part 1. Effect of particle volume fraction and size. J Mater Sci 1984;19:473–86.
[26] Spanoudakis J, Young RJ. Crack propagation in a glass particle-filled epoxy resin. Part 2. Effect of particle–matrix adhesion. J Mater Sci 1984;19:487–96.
[27] Moloney AC, Kausch HH, Kaiser T, Beer HR. Review—Parameters determining the strength and toughness of particulate filled epoxide resins. J Mater Sci 1987;22:381–93.
[28] Nakamura Y, Okabe S, Iida T. Effects of particle shape, size and interfacial adhesion on the fracture strength of silica-filled epoxy resin. Polym Polym Compos 1999;7(3):177–86.
[29] Nakamura Y, Yamaguchi M. Effects of particle size on the fracture toughness of epoxy resin filled with spherical silica. Polymer 1992;33(16):3415–26.
[30] Tippur HV, Krishnaswamy S, Rosakis AJ. Optical mapping of crack tip deformations using the methods of transmission and reflection coherent gradient sensing: a study of crack tip *K*-dominance. Int J Fract 1991;52:91–117.
[31] Krishnaswamy S, Tippur HV, Rosakis AJ. Measurement of transient crack-tip deformation fields using the method of coherent gradient sensing, *K*-dominance. J Mech Phys Solids 1992;40(2):339–72.
[32] Faber KT, Evans AG. Crack deflection process—I. Theory. Acta Metall 1983;31(4):565–76.
[33] Anderson TL. Fracture mechanics, fundamentals and applications. 2nd ed. CRC Press; 1995. p. 603–5.